nature communications

Article

https://doi.org/10.1038/s41467-023-38649-5

Wigner-molecularization-enabled dynamic nuclear polarization

Received: 3 August 2022

Accepted: 10 May 2023

Published online: 23 May 2023

Check for updates

Wonjin Jang[1], Jehyun Kim[1], Jaemin Park[1], Gyeonghun Kim[1], Min-Kyun Cho[1], Hyeongyu Jang[1], Sangwoo Sim[1], Byoungwoo Kang[1], Hwanchul Jung[2], Vladimir Umansky[3] & Dohun Kim[1]

Multielectron semiconductor quantum dots (QDs) provide a novel platform to study the Coulomb interaction-driven, spatially localized electron states of Wigner molecules (WMs). Although Wigner-molecularization has been confirmed by real-space imaging and coherent spectroscopy, the open system dynamics of the strongly correlated states with the environment are not yet well understood. Here, we demonstrate efficient control of spin transfer between an artificial three-electron WM and the nuclear environment in a GaAs double QD. A Landau–Zener sweep-based polarization sequence and low-lying anticrossings of spin multiplet states enabled by Wigner-molecularization are utilized. Combined with coherent control of spin states, we achieve control of magnitude, polarity, and site dependence of the nuclear field. We demonstrate that the same level of control cannot be achieved in the non-interacting regime. Thus, we confirm the spin structure of a WM, paving the way for active control of correlated electron states for application in mesoscopic environment engineering.

Semiconductor quantum dot (QD) systems facilitate investigations of the interaction between electron spins and nuclear environments, which is known as the central-spin problem[1,2]. Although the fluctuation of nuclear fields, which is quantified by the effective Overhauser field B_{nuc}[3,4], often acts as a magnetic-noise source for spin qubits[3], the hyperfine electron–nuclear spin interaction allows achieving dynamic nuclear polarization (DNP)[5–8]. DNP is used for enhancing the signal-to-noise ratio in nuclear magnetic resonance[6] and prolonging coherence times in QD-based spin qubits[9,10]. Gate-defined semiconductor QDs have been used to achieve the fast probing of nuclear environments[8,11,12], bidirectional DNP[11], and active feedback control of nuclear fields[10].

While the DNP achieved by spin-flip mediated transport with an applied bias[13,14] allows large DNP[13], the QD - reservoir tunnel rate needs to be large enough to allow the finite spin-flip current. On the contrary, the DNP based on the pulsed-gate technique can be demonstrated while maintaining the small tunnel rates ~10^1 kHz. Because the qubit control typically requires small QD-reservoir tunnel rates transition from the pulsed-gate DNP to qubit experiments is straightforward without additional parameter modulation via the gate voltages. However, spin qubit control combined with DNP has been limited to two-electron singlet–triplet (ST_0) spin qubits[9–12,15]. Despite the versatility of gate-defined QD systems[16–19], the large singlet–triplet energy splitting E_{ST} (~10^2 h·GHz; h is Planck's constant) in particular in GaAs limits the access to higher spin states[20] in multielectron QDs at moderate external magnetic fields $B_0 < 1$ T or within a typical frequency bandwidth of experimental setups.

Coulomb-correlation-driven Wigner molecules (WMs) in confined systems[21–25] may provide new directions for expanding nuclear control to multielectron systems. Recent studies on QDs in various systems have shown clear evidence of WM formation[22,23,25–29]. It has been demonstrated that the E_{ST} can reach down to ~10^0 h·GHz upon the WM formation[27,29] because of strong electron–electron interactions confirmed by full-configuration interaction (FCI)-based theories[23,25,28,30].

[1]Department of Physics and Astronomy, and Institute of Applied Physics, Seoul National University, Seoul 08826, Korea. [2]Department of Physics, Pusan National University, Busan 46241, Korea. [3]Braun Center for Submicron Research, Department of Condensed Matter Physics, Weizmann Institute of Science, Rehovot 76100, Israel. e-mail: dohunkim@snu.ac.kr

However, most studies have focused on the spectroscopic confirmation of WM formation, and studies on the open system dynamics using correlated states have not been reported to date.

Here, we demonstrate the formation of a WM in semiconductor QDs, which helps achieving efficient spin environment control. We use gate-defined QDs in GaAs and exploit the quenched energy spectrum of the WM (E_{ST} ~ 0.9 h·GHz) to enable mixing between different spin subspaces within $B_0 < 0.3$ T. Furthermore, we demonstrate DNP by pulsed-gate control of the electron spin states. Leakage spectroscopy and Landau–Zener–Stuckelberg (LZS) oscillations confirm a sizable bidirectional change in B_{nuc} ~ 80 mT and the spatial Overhauser field gradient ΔB_{nuc} ~ 35 mT due to the long nuclear spin diffusion time τ_N ~ 62 s. Further, we demonstrate on-demand control of B_{nuc} combined with coherent LZS oscillations, providing a new route for realizing controllable DNP using correlated electron states.

Results

Figure 1a shows a gate-defined QD device fabricated on a GaAs/AlGaAs heterostructure, where a 2D electron gas (2DEG) is formed ~70 nm below the surface (see Methods). We focus on the left double QD (DQD) containing three electrons. We designed the V_2 gate to form an anisotropic potential, which is predicted to promote WM formation[22]. An electrostatic simulation of the electric potential at the QD site near V_2 shows an oval-shaped confinement potential with anisotropy

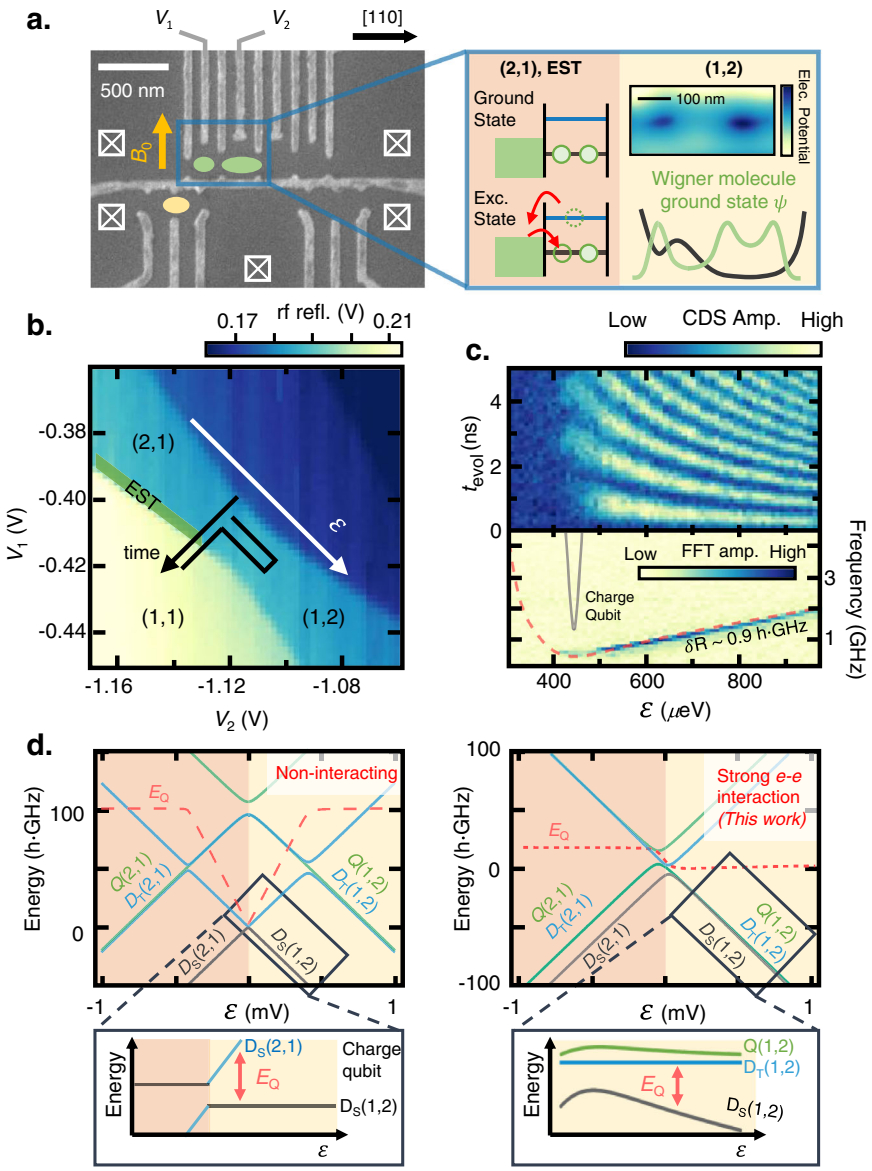

Fig. 1 | Wigner molecule formation in a GaAs double quantum dot. a Scanning electron microscope image of a GaAs quantum dot (QD) device similar to the one used in the experiment. Green dots denote the double QD defined for Wigner molecule (WM) formation which is aligned along the [110] crystal axis (black arrow). The inner plunger gate V_2 is designed to have anisotropic confinement potential as shown in the right panel to facilitate the localization of the electronic ground state. Yellow circle: a radio-frequency (rf) single-electron transistor (rf-SET) charge sensor for rf-reflectometry. External magnetic field B_0 is applied along the direction denoted by the yellow arrow. **b** Charge stability diagram of the double QD near the three-electron region spanned by V_1 and V_2 gate voltages. Green-shaded region: the energy-selective tunneling (EST) position for the state readout and initialization. **c** Landau–Zener–Stückelberg (LZS) oscillation of the WM at $B_0 = 0$ T. The relative phase evolution between the excited doublet (D_T) and the ground doublet (D_S) results in the oscillation captured by the EST readout. Red-dashed curve in the fast Fourier transformed (FFT) map shows energy dispersion calculated from the toy-model Hamiltonian. The calculation yields quenched orbital energy spacing of the inner dot δR ~ 0.9 h·GHz. **d** Left (Right) panel: Energy spectrum along the (2,1)–(1,2) charge configuration in the non-interacting (strongly interacting, this work) regime with δL ~ 100 h·GHz (δL ~ 19 h·GHz), and δR ~ 100 h·GHz (δR ~ 0.9 h·GHz). E_Q (red-dashed curve) is the energy splitting between the two lowest levels.

exceeding 3 (Fig. 1a, right panel). This potential can be tuned by the gate voltage, allowing the controlled electron correlation and localization of the ground state wavefunction within the DQD[22,24,26,27]. The yellow dot in Fig. 1a. denotes a radio-frequency single-electron transistor (rf-SET) charge sensor utilized for quantum state readout[31–33]. The device was operated in a dilution refrigerator with a base temperature of ~40 mK, an electron temperature T_e ~ 150 mK (Supplementary Note 1), and a variable B_0 applied to the direction shown in Fig. 1a.

The three-electron DQD results in two spin doublets and one spin quadruplet state. Without the magnetic field in the (2,1) [(1,2)] charge configuration, doublet-singlet state $D_S(2,1)$ [$D_S(1,2)$] with total spin $S = 1/2$ form the ground state where the two electrons in the left [right] QD form a spin singlet state and fill the ground orbital in the left [right] QD. Here, n [m] denotes the number of electrons in the left [right] QD by (n, m). When the two electrons in the left [right] QD form a spin triplet state and fill the excited orbital in the left [right] QD, the three-electron state result in either the doublet-triplet state $D_T(2,1)$ [$D_T(1,2)$] with $S = 1/2$ or the quadruplet state $Q(2,1)$ [$Q(1,2)$] with $S = 3/2$. Because of the orbital splitting, the D_T, and Q states usually have higher energy compared to D_S states[34–36]. If a finite magnetic field is applied, doublet states with $S = 1/2$ are split into $m_s = +1/2$ and $-1/2$ states whereas quadruplet states with $S = 3/2$ are split into $m_s = +3/2, +1/2, -1/2$, and $-3/2$ states. Here m_s is the spin quantum number related to the z component of the electron spin angular momentum. The explicit spin structures are shown in the Methods. Hereafter, (n, m; m_s) notation is used to describe both the charge configuration and spin angular momentum of a state.

First, we show the spectroscopic evidence of the WM at $B_0 = 0$ T by probing E_{ST} in the right QD δR. Figure 1b shows a charge stability diagram around (2,1) and (1,2). The green-shaded region near the (2,1)−(1,1) charge transition is exploited for energy-selective tunneling (EST) readout and state initialization[27,37,38]. We tune the electron tunneling-in (-out) time τ_{in} (τ_{out}) of the left dot to 14 (7) μs. Starting from the initialized ground doublet state D_S in the (2,1) charge configuration, we apply non-adiabatic pulses (Fig. 1b) simultaneously to V_1 and V_2 with a rise time of ~500 ps and a repetition period of 51 µs ≫ τ_{in} to induce coherent LZS oscillation[39,40]. The oscillation reveals the relative phase evolution between the excited and ground doublet states (D_T and D_S), the frequency of which is governed by δR.

Figure 1c shows the resultant LZS oscillations as a function of evolution time t_{evol} and detuning ε. The E_{ST} in GaAs DQDs in the non-interacting regime is typically on the order of 10^2 h.GHz[20] (Fig. 1d). In a charge qubit regime, a steep rise in the LZS oscillation frequency $f_{LZS} \sim E_Q/h$ as a function of ε (Fig. 1c, black curve) and short coherence time $T_2^* \sim 10$ ps due to strong susceptibility to charge noise is expected[41]. E_Q is the energy splitting between the two lowest levels (Fig. 1d, red-dashed curve). However, we find a significantly smaller f_{LZS} in the (1,2) charge configuration and $T_2^* \sim 10$ ns because of the reduced dispersion of f_{LZS} versus ε. This is reminiscent of a QD hybrid qubit[27,40,42], but the excited energy is suppressed owing to the electron–electron interaction. WM formation in our previous GaAs device has been recently confirmed by FCI calculation[27,28,30]. Although such calculation is needed to rigorously determine parameters, we roughly estimate $\delta R \sim 0.9$ h.GHz, by fitting the fast Fourier transformed (FFT) spectrum to the calculation result (Fig. 1c, red-dashed curve) derived from a toy-model Hamiltonian[37,39,40] (see Supplementary Note 2).

The full energy spectrum calculation of the three-electron states using the parameters obtained experimentally across the (2,1)−(1,2) configuration is illustrated in Fig. 1d (right panel). The suppressed E_{ST} of the left dot $\delta L \sim 19$ h·GHz is obtained by measuring the width of the EST region in the charge stability diagram with the lever arm of the gate $V_1 \sim 0.03$. The left QD also allows a weak Wigner molecularization as the measured δL is an order of magnitude smaller than the case of non-interacting regime. Because of the small value of $\delta L/(k_B T_e) \sim 6$, where k_B is Boltzmann's constant, thermal tunneling precludes high-fidelity single-shot readout. We obtain data by the time-averaged signal using the correlated-double sampling (CDS) method, which effectively yields the signal proportional to the excited state probability[37] (see Supplementary Note 3).

We confirm the WM spin structure via the strongly suppressed energy spectrum in the right QD with varying B_0. We focus on five low-lying energy levels among eight possible multiplet states. See Methods for notations used for labeling spin multiplets. As shown in Fig. 2a (left panel), $D_S(1,2;-1/2)$ [$D_S(1,2;1/2)$] becomes degenerate with $D_T(1,2;1/2)$ or $Q(1,2;1/2)$ [$Q(1,2;3/2)$] at a certain ε depending on the B_0 magnitude. The degeneracies are lifted by the transverse Overhauser field $B_{nuc}^{\perp}$ [8,11]. To detect such anticrossings, we first initialize the state to either $D_S(2,1;-1/2)$ or $D_S(2,1;1/2)$ at the EST position. By pulsing the initialized $D_S(2,1;-1/2)$ [$D_S(2,1;1/2)$] towards (1,2) and holding for ~100 ns ≫ T_2^*, mixing with (or leakage to) states $Q(1,2;1/2)$ or $D_T(1,2;1/2)$ [$Q(1,2;3/2)$] can occur if the pulse amplitude A_p coincides with the anti-crossing position (Fig. 2a, right panel). Upon pulsing back to the (2,1) charge configuration, the resultant excited states Q or the D_T probability can be detected via EST[27,37,38]. Figure 2b shows the leakage spectrum versus A_P and B_0, mapping out the anti-crossing positions similar to "spin-funnel" measurements in two-electron ST_0 qubits reproducing the energy splittings between the ground and excited levels[8,16,43,44]. The black (red) dashed curves show the calculated splittings (Fig. 1d) between the D_S and D_T (Q) states at $B_0 = 0$ T, with the Lande g-factor $g^* \sim -0.4$ [45,46].

Although the calculated curve qualitatively agrees with the experimental curve, the observed spectrum curvature as a function of A_P and B_0 is smaller because of the DNP induced by the pulse sequence used for leakage spectroscopy. To confirm this, before each line scan of A_p in Fig. 2c, d, a similar step pulse with a fixed amplitude $A_P' \sim 370$ mV (450 mV) is applied for 10 s. Consequently, we observe distortions (red circles) in the spectrum occurring at A_P'. This is because, when A_P' matches with the anti-crossing position, the pulse probabilistically flips the electron spin with a change in the angular momentum $\Delta m_S = +1$ by the leakage process described above and accompanies flop $\Delta m_N = -1$ of the nuclear spin[8,11]. Unlike the electrons in GaAs, nuclei have positive g-factors[8,20]; therefore, the $\Delta m_S = +1$ electron spin flip, and thereby the $\Delta m_N = -1$ nuclear spin flip polarizes B_{nuc} toward the B_0 direction[8,11,47]. This additionally drags the leakage spectrum opposite to the B_0 direction under a specific condition $A_p = A_P'$. These results indicate that leakages induced by hyperfine interaction between the WM and nuclear environment lead to an observable change in B_{nuc}. Despite the long measurement time per line scan (~7 s) owing to the communication latency between the measurement computer and the instruments, the polarization effect is still visible. Thus, $\tau_N > 10$ s, as discussed below. Moreover, as the anti-crossing position is a sensitive function of $B_{tot} = B_0 + B_{nuc}$ over 100-300 mT, it can be used to measure B_{nuc}.

We now show bidirectional DNP combined with coherent control of doublet states at $B_0 = 230$ mT. Figure 3a (top panel) shows the three primary paths through the anticrossings, which can flip the electron spins deterministically by adiabatic passage[2,8,11]. Paths P_1 and P_3 describe the S-polarization that flips the electron spin with $\Delta m_S = +1$. This is enabled by initializing the state to $D_S(1,2;-1/2)$ [$D_S(1,2;1/2)$] at the EST position and then by non-adiabatically pulsing beyond the first anticrossings near the (2,1) charge configuration (Fig. 3a, yellow boxes), followed by adiabatically driving the state through the anti-crossing to $Q(1,2;1/2)$ [$Q(1,2;3/2)$], which accompanies $\Delta m_N = -1$ (Fig. 3a, blue arrows). Because the spin state is initialized to the doublet-singlet state before the adiabatic spin-flip passage, the sequence is named S-polarization. The $Q(1,2;1/2)$ [$Q(1,2;3/2)$] state is diabatically driven back to the EST position, and one electron quickly tunnels out to the reservoir. Reloading an electron from the reservoir reinitializes one of the Ds states completing the polarization cycle. Both the $D_S(1,2;-1/2)$ and $D_S(1,2;1/2)$ initial states contribute to the S-polarization. Path P_2 denotes the T-polarization ($\Delta m_S = -1$, $\Delta m_N = +1$),

https://doi.org/10.1038/s41467-023-38649-5

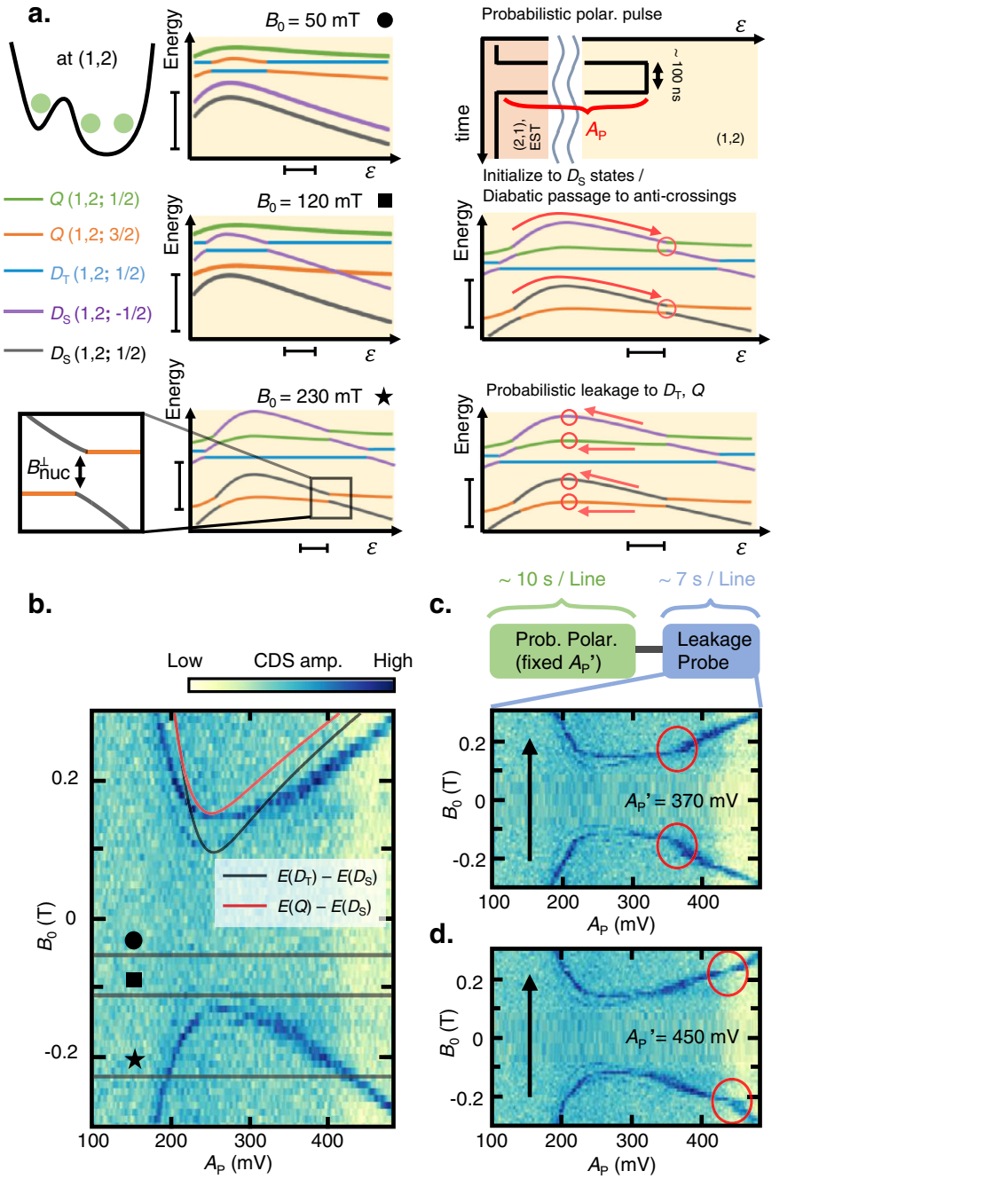

Fig. 2 | Leakage spectroscopy and probabilistic nuclear polarization with the Wigner molecule. a Left panel: schematics of the energy levels for different external magnetic fields $B_0 > 0$ T. Crossings between different m_s states become anticrossings aided by the transverse nuclear Overhauser field. Right panel: schematic of the pulse sequence for leakage spectroscopy and probabilistic dynamic nuclear polarization (DNP). The pulse diabatically drives the initialized $D_S(2,1;1/2)$ [$D_S(2,1;-1/2)$] to (1,2), and hold ε for 100 ns $\gg T_2^*$. Upon the coincidence of the pulse detuning and the anti-crossing, the state probabilistically evolves to $Q(1,2;3/2)$ [$Q(1,2;1/2)$] and flips the electron spin $\Delta m_S = +1$ which accompanies $\Delta m_N = -1$. The scale bars on the bottom axis (ε axis) denote 50 μeV, and the scale bars on the left axis (Energy axis) denote 1 h·GHz. **b** Leakage spectroscopy of the Wigner molecule (WM) state as a function of B_0 and the pulse amplitude A_P. Black (Red) dotted curve shows the calculated energy splitting between D_T (Q) and D_S at $B_0 = 0$ T. Measurement-induced nuclear field shifts the dispersion opposite to the direction of B_0. **c**, **d** Leakage measurement with an additional probabilistic polarization pulse with amplitude A_P' applied before each line sweep. The A_P' is fixed to 370 (450) mV, and the additional distortion in the leakage spectrum is shown as red circles near a pulse amplitude of 370 (450) mV. Black arrows denote the magnetic field sweep direction.

which is possible by driving $D_T(1,2;1/2)$ adiabatically to $D_S(1,2;-1/2)$ (Fig. 3a, red arrow). To prepare $D_T(1,2;1/2)$, we apply a π-pulse to $D_S(2,1;1/2)$ before the adiabatic passage (Fig. 3a, bottom panel). Because we prepare the doublet-triplet state before the adiabatic spin-flip passage, the sequence is called T-polarization. The T-polarization is possible only when the state is initialized to $D_S(2,1;1/2)$ at the EST position.

Combining the S- and T-polarizations, we measure the change in B_{nuc} (δB_{nuc}), where the repeated polarization pulse sequence (Fig. 3a, bottom panel) with variable t_{evol} and a repetition rate of ~20 kHz is applied for 10 s before each line scan. For Fig. 3b, a waiting time ~10 min was added after each sweep to allow the polarized nuclei to diffuse and minimize the polarization effect in the next sweep. As shown in Fig. 3b, δB_{nuc} oscillates with t_{evol}, which is anti-

https://doi.org/10.1038/s41467-023-38649-5

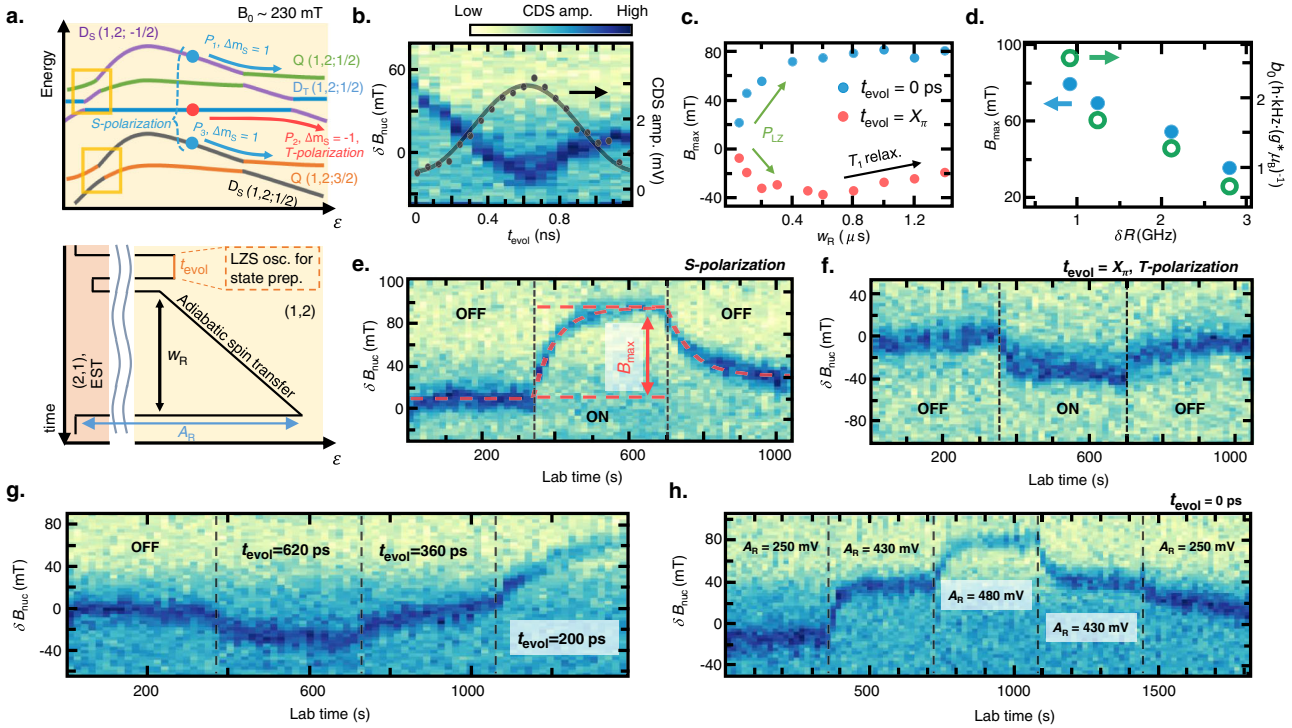

Fig. 3 | Bidirectional and controllable dynamic nuclear polarization enabled by Wigner molecularization. a Top panel: Schematic of the anticrossings used for deterministic dynamic nuclear polarization (DNP). Bottom panel: pulse sequence used for S- and T-polarizations. For $t_{evol} = 0$ ns, the sequence corresponds to maximum S-polarization, which brings $D_S(1,2;1/2)$ [$D_S(1,2;-1/2)$] adiabatically across the anti-crossing to $Q(1,2;3/2)$ [$Q(1,2;1/2)$] flipping the electron spin with $\Delta m_S = +1$ and leading to $\Delta m_N = -1$ (blue arrow, S-polarization). For $t_{evol} = 600$ ns, the sequence corresponds to maximum T-polarization. Herein, the $D_T(1,2;1/2)$ prepared with a (Landau–Zener–Stückelberg) LZS-oscillation-induced π-pulse is adiabatically transferred to $D_S(1,2;1/2)$, resulting in $\Delta m_S = -1$ and $\Delta m_N = +1$ (red arrow, T-polarization), which has the opposite polarization effect compared to S-polarization. **b** Change in the nuclear field δB_{nuc} as a function of t_{evol}. The gray curve shows the corresponding LZS oscillation measurement reflecting the D_T population. The δB_{nuc} oscillates out of phase to the LZS oscillation owing to the oscillation of the S- and T-polarization ratio. **c** The magnitude of the maximum polarization B_{max} as a function of ramp time w_R. The B_{nuc} saturates to B_{max} when the polarization and the nuclear spin diffusion rate reach an equilibrium. For small w_R, the $|B_{max}|$ decreases because of the small Landau–Zener transition probability P_{LZ} for both S- (blue circle) and T-polarizations (red circle). In the case of T-polarization, $|B_{max}|$ decreases again for long w_R owing to the lattice relaxation of the excited population. **d** B_{max} as a function of δR. The polarization gets more efficient for smaller δR indicating a strong dependence of the nuclear polarization efficiency on the Wigner parameter. **e, f** Dynamic nuclear control with the S (T)-polarization sequence. The red dotted line is the numerical fit derived from the simple rate equation-based model. The fit yields the nuclear spin diffusion time $\tau_N \sim 62$ s, with a polarization magnitude per spin flip of ~2.58 h·kHz·$(g^*\mu_B)^{-1}$. **g** On-demand DNP via t_{evol}. **h** Adiabatic ramp amplitude A_R with $t_{evol} = 0$ ns realizing self-limiting DNP.

correlated with the LZS oscillation that represents the population of $D_T(1,2;1/2)$. This confirms that the net polarization rates can be controlled by adjusting t_{evol}. Accordingly, we calibrate $t_{evol} = 0$ (0.62 ns) for S (T)-polarization. We also calibrate the duration of the adiabatic spin transfer w_R. Figure 3c shows the maximum nuclear field change B_{max} reachable as a function of w_R, where both S- and T-polarizations are ineffective for short w_R because of negligible adiabatic transfer probability P_{LZ}[2,48]. $|B_{max}|$ reaches a maximum around $w_R \sim 0.8$ μs, after which the maximum efficiency is retained for the S-polarization sequence. In the case of T-polarization, however, for long w_R, $|B_{max}|$ decreases because of D_T relaxation during the adiabatic passage.

By tuning δR via the dc gate voltages and performing similar S-polarization experiments, we find that B_{max} decreases with increasing δR (Fig. 3d, see Supplementary Note 4). As is discussed subsequently, we find that the nuclear diffusion time scale exceeds 60 s regardless of δR, but the Overhauser field change per electron flip b_0 is strongly suppressed with increasing δR. Ultimately, the observation implies that the pulsed-gate-based nuclear control becomes inefficient in the non-interacting regime. We suspect the degree of electronic wavefunction localization which depends on the Wigner parameter may be affecting the contact hyperfine interaction between the electron and the nuclear spins and altering the DNP efficiency as a result.

Returning to the condition $\delta R \sim 0.9\ h$·GHz, we demonstrate on-demand DNP. Figure 3e, f shows the result of optimized S (T)-polarization with $t_{evol} = 0$ ns, $w_R = 1000$ ns ($t_{evol} = 0.62$ ns, $w_R = 600$ ns). Although the local fluctuations of the nuclear spins lead to random drift of the anti-crossing positions without the polarization pulse, B_{nuc} builds toward (opposite to) the B_0 direction faster than the nuclear spin diffusion timescale when the polarization pulse is applied before each line scan. δB_{nuc} rises to B_{max} 80 mT (−40 mT) until a dynamic equilibrium is reached. Because only the $m_s = 1/2$ states contribute to the T-polarization, $|B_{max}|$ for the T-polarization is about half of that for the S-polarization, implying that the state initialize to both m_s states with nearly equal probability at the EST position.

We also demonstrate bidirectional DNP by adjusting t_{evol} in Fig. 3g. Figure 3h illustrates the control of B_{nuc} by adjusting the adiabatic sweep amplitude A_R of the S-polarization sequence. Under the S-polarization, B_{nuc} builds in the B_0 direction and drives the anti-crossing to deeper ε (more to (1,2) charge configuration). Because the pulse cannot have a finite polarization effect if the anti-crossing position is driven beyond ε reachable with A_R, A_R serves as the limiting factor of B_{max}. Thus, a self-limiting DNP protocol, where the DNP field is limited by experimental parameters used in the pulse shape rather than the interplay between pumping rate and nuclear diffusion, can be realized. This self-limiting property can be useful in future DNP experiments as the steady state DNP field can be simply controlled by adjusting the pulse amplitude.

Using a simple rate equation, we simulate the polarization-probe sequence (red-dashed curve in Fig. 3e, see Methods and Supplementary Note 5) and obtain $\tau_N \sim 62$ s and $b_0 \sim 2.58\ h{\cdot}\mathrm{kHz}{\cdot}(g^*\mu_B)^{-1}$ from the fit. In contrast, the DNP effect is negligible in our device with the two-electron ST_0 qubit[8] under the same repetition rate as in the WM regime (see Supplementary Note 6). We further find our DNP is still effective when the repetition rate is as low as 5 kHz (see Supplementary Note 7) showing that the Wigner molecule allows sizable DNP that cannot be achieved with conventional QDs. Through optimization of the magnitude and direction of B_0, $b_0 \sim 3\ h\,\mathrm{kHz}{\cdot}(g^*\mu_B)^{-1}$ can be achieved with an ST_0 qubit in GaAs[2,8]. However, the obtained result shows that robust nuclear control can be achieved with WMs even in the regime where the same level of control cannot be achieved with an ST_0 qubit. In addition, residual polarization ~21.5 mT exists after turning off the polarization sequence (Fig. 3e), which diffuses within ~30 min. The large Knight shift gradient originating from the non-uniformly broadened WM wavefunction may be a possible cause of the long τ_N. However, the newly observed phenomena in this study, including the dependence of b_0 on the tuning condition, require further investigations[47,49].

Furthermore, the WM's coherent LZS dynamics provide a novel approach to measure the spatial Overhauser field gradient ΔB_Z between QDs. When ΔB_Z is larger than the exchange splitting between $D_T(1,2;1/2)$ [$D_T(1,2;-1/2)$] and $Q(1,2;1/2)$ [$Q(1,2;-1/2)$], the eigenstates are expected to become $D_{T1}(1,2;1/2) = |\downarrow\rangle|T_+\rangle$ [$D_{T1}(1,2;-1/2) = |\uparrow\rangle|T_-\rangle$] and $D_{T0}(1,2;1/2) = |\uparrow\rangle|T_0\rangle$ [$D_{T0}(1,2;-1/2) = |\downarrow\rangle|T_0\rangle$][35]. Because both states can tunnel-couple to $D_S(1,2;1/2)$ [$D_S(1,2;-1/2)$], the LZS oscillation reveals the $D_{T1} - D_S$ and $D_{T0} - D_S$ energy splittings. As can be inferred from the Hamiltonian (see Supplementary Note 8), although the $D_{T0} - D_S$ splitting is independent of the ΔB_Z and B_Z, the $D_{T1} - D_S$ splitting is modulated by ΔB_Z depending on the sign of ΔB_Z and m_s, providing the direct measure of ΔB_Z. Because the states can initialize to both $D_S(1,2;1/2)$ and $D_S(1,2;-1/2)$ at the EST position, the LZS oscillation captures the dynamics of both $m_s = 1/2$ and $m_s = -1/2$ subspaces.

Figure 4a (4b) illustrates the LZS oscillation measurement of the WM multiplet states at $B_0 = 230$ mT in the time (frequency) domain with the S-polarization turned on and off at specific laboratory times. The FFT spectrum exhibits three different branches corresponding to the $D_{T0} - D_S$ (red arrow) and $D_{T1} - D_S$ (black and black-dashed arrows) where the beating patterns vary as the S-polarization induces changes in ΔB_z. Two different $D_{T1} - D_S$ branches correspond to different m_s subspaces, where the sign of ΔB_z should be known to distinguish the m_s for each branch. The $D_{T0} - D_S$ splitting is the same for both m_s subspaces and is displayed as a single branch (red arrow). Figure 4c, d shows the simulated time (frequency) domain signal of the same LZS oscillation, which agrees well with the experimental result (see Supplementary Note 9). As expected, the $D_{T0} - D_S$ splitting is constant regardless of ΔB_z, whereas the $D_{T1} - D_S$ splitting is modulated along the polarization sequence.

The $D_{T0} - D_{T1}$ splitting without the polarization sequence implies the built-in $\Delta B_z \sim 200\ h{\cdot}\mathrm{MHz}{\cdot}(g^*\mu_B)^{-1}$ (35 mT), which is also confirmed by the ST_0 oscillation (see Supplementary Note 6). ΔB_z increases to $400\ h{\cdot}\mathrm{MHz}{\cdot}(g^*\mu_B)^{-1}$ (70 mT) with the S-polarization and decreases to $200\ \mathrm{h\,MHz}{\cdot}(g^*\mu_B)^{-1}$ after turning the polarization off. Thus, we conclude that the S-polarization yields the asymmetric pumping effect ($\Delta B_{nuc} \sim 200\ \mathrm{h\,MHz}{\cdot}(g^*\mu_B)^{-1}$) about the QD sites, whereas the ΔB_{nuc} direction can be experimentally checked, for example, via single-spin electric-dipole spin resonances[46]. Furthermore, the $D_{T0} - D_S$ splitting comprises the decoherence-free subspace for the qubit operations resilient to magnetic noises, where the coherent microwave control combined with the large polarization may enable leakage-free and state-selective transitions.

Discussion

The present work uncovers the spin and energy structure of the WM states and explores the central-spin problem with strongly correlated WM states in semiconductor QDs. With the energy splitting of the WM ~ 0.9 h·GHz, we confirm the controllable DNP of B_{nuc} (ΔB_{nuc}) reaching (but not limited to) 80 mT (35 mT) via leakage spectroscopy and LZS oscillations. The τ_N exceeds 60 s, which, together with bidirectional polarizability, is beneficial for stabilizing the nuclear bath fluctuation and realizing long-lived nuclear polarization[10,15].

We anticipate several directions for further developments and applications of WM-enabled DNP. Similar experiments with a larger $\delta L/T_e$ ratio can enable high-fidelity single-shot readout for a faster measurement of the dynamics of nuclear polarization. This would further enable feedback loop control[10] and tracking[12,50,51] of nuclear environments in multielectron QDs which can be utilized to narrow the nuclear field distribution for electron coherence enhancement. The real-time Hamiltonian estimation also improves frequency resolution for measuring instantaneous ΔB_{nuc}, which may enable measurements of the degree of spatial localization within WMs. We expect more asymmetric QD geometry would allow a smaller energy gap and thereby the broader electronic wavefunction. Along with the tunability of the energy gap via the gate voltage, as shown here, this may facilitate the investigation of the spatial noise characteristics within a single QD which has been impractical with the typical QD geometries. Furthermore, DNP becomes inefficient with increasing E_{ST} of the WM, as discovered herein. This implies that the pulsed-gated electron–nuclear flip-flop probability is a strong function of the Wigner parameter, the microscopic origin of which requires more rigorous investigations.

Methods

Device fabrication

A quadruple QD device was fabricated on a GaAs/AlGaAs heterostructure with a 2DEG formed ~70 nm below the surface. The transport property of the 2DEG showed mobility $\mu = 2.6 \times 10^6\ \mathrm{cm^2(V\,s)^{-1}}$ with electron density $n = 4.0 \times 10^{11}\ \mathrm{cm^{-2}}$ at temperature $T = 4$ K. Electronic mesa around the QD site was defined by the wet etching technique, and thermal diffusion of a metallic stack of Ni/Ge/Au was used to form the ohmic contacts. The depletion gates were deposited on the surface using standard e-beam lithography and metal evaporation of 5 nm Ti/30 nm Au. The lithographical width of the inner QD along the QD axis direction was designed to be ~10% wider than the outer dot to facilitate WM formation. The QD array was aligned to the [110] crystal axis, as shown in Fig. 1a. Although the magnetic field B_0 was intended to be applied perpendicular to the [110] axis to minimize the effect of spin-orbit interaction[2], the angular deviation was not strictly calibrated.

Measurement

The device was placed on a ~40 mK plate in a commercial dilution refrigerator (Oxford instruments, Triton-500). Ultra-stable dc-voltages were generated by battery-powered dc-sources (Stanford Research Systems, SIM928). They were then combined with rapid voltage pulses from an arbitrary waveform generator (AWG, Keysight M8195A with a sample rate up to 65 GSa/s) via homemade wideband (10^1–10^{10} Hz) bias tees to be applied to the metallic gate electrodes. An LC-tank circuit with a resonant radio frequency (rf) of ~120 MHz was attached to the ohmic contact near the SET charge sensor to enable high-bandwidth ($f_{BW} > 1$ MHz) charge detection[27,31–33,37]. The reflected rf-signal was first amplified by 50 dB using two-stage low-noise cryo-amplifiers (Caltech Microwave Research, CITLF2 ×2 in series) at a 4 K plate. Next, it was further amplified by 25 dB at room temperature using a homemade low-noise rf-amplifier. The signal was then demodulated by an ultra-high-frequency lock-in amplifier (Zurich Instruments, UHFLI), which was routed to the boxcar integrator built in the UHFLI. Trigger signals with a repetition period of 51 μs were generated by a field-programmable-gate array (FPGA, Digilent, Zedboard) to synchronize the timing of the AWG and the boxcar integrator for the CDS[37].

https://doi.org/10.1038/s41467-023-38649-5

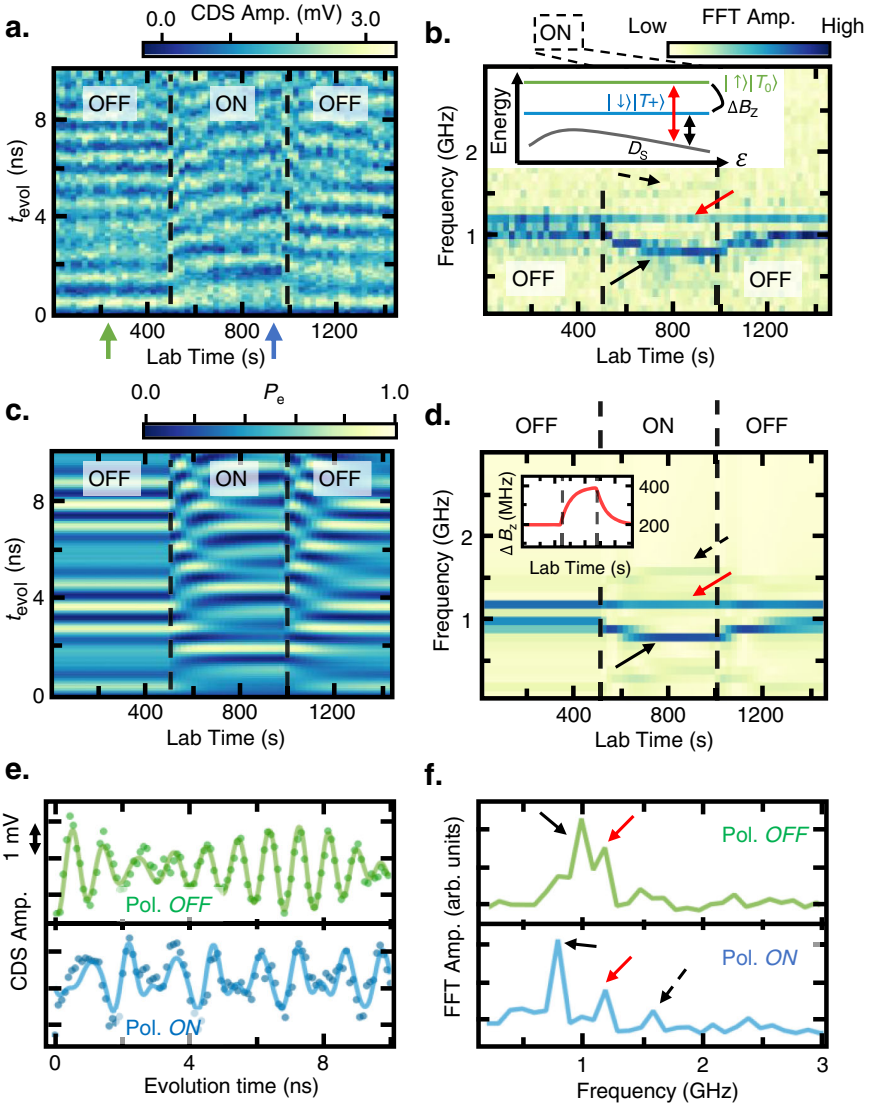

Fig. 4 | Field gradient control and measurement. Landau–Zener–Stückelberg (LZS) oscillation of the Wigner molecule (WM) states at $B_0 = 230$ mT in **a** the time domain and **b** the frequency domain with the S-polarization sequence. The oscillation reveals the relative phase oscillation of the $D_{T1} - D_S$ (black arrow, black dotted arrow) and $D_{T0} - D_S$ (red arrow) of both the $m_s = 1/2$ and $m_s = -1/2$ states. The $D_{T0} - D_S$ splitting is constant regardless of the magnetic field gradient ΔB_Z, whereas the $D_{T1} - D_S$ energy spacing is modulated by the ΔB_Z depending on the sign of ΔB_Z and m_s. The resultant beating is visible in **e**, **f** the time (frequency) domain line-cut when the polarization is on (green arrow in **a**) and off (blue arrow in **a**). The line cuts in the time domain are numerically fitted to the sum of three sine functions (solid lines in **e**) with different amplitudes. Three separate peaks are visible in the frequency domain (**f**) when the ΔB_Z is largely polarized in the bottom panel (blue line) in (**f**) Simulated LZS oscillation in **c** the time domain and **d** the frequency domain with the ΔB_Z in the inset of (**d**). The simulation in the frequency domain reproduces the branches shown in (**b**).

Table 1 | Three-electron spin states

State	Spin structure
$Q(1,2; m_s = 3/2)$	$\lvert\uparrow\rangle\lvert T_+\rangle$
$Q(1,2; m_s = 1/2)$	$\frac{1}{\sqrt{3}}[\sqrt{2}\lvert\uparrow\rangle\lvert T_0\rangle + \lvert\downarrow\rangle\lvert T_+\rangle]$
$Q(1,2; m_s = -1/2)$	$\frac{1}{\sqrt{3}}[\sqrt{2}\lvert\downarrow\rangle\lvert T_0\rangle + \lvert\uparrow\rangle\lvert T_-\rangle]$
$Q(1,2; m_s = -3/2)$	$\lvert\downarrow\rangle\lvert T_-\rangle$
$D_S(1,2; m_s = 1/2)$	$\lvert\uparrow\rangle\lvert S\rangle$
$D_T(1,2; m_s = 1/2)$	$\frac{1}{\sqrt{3}}[\lvert\uparrow\rangle\lvert T_0\rangle - \sqrt{2}\lvert\downarrow\rangle\lvert T_+\rangle]$
$D_S(1,2; m_s = -1/2)$	$\lvert\downarrow\rangle\lvert S\rangle$
$D_T(1,2; m_s = -1/2)$	$\frac{1}{\sqrt{3}}[\lvert\downarrow\rangle\lvert T_0\rangle - \sqrt{2}\lvert\uparrow\rangle\lvert T_-\rangle]$

Here, T_0, T_+ and T_- denote the three triplet states ($S = 1$) with $m_s = 0$, +1 and −1 respectively and S indicates the spin singlet state ($S = 0$).

Eigenstates of three-electron spin states

Three-electron spin-multiplet structure consists of eight different eigenstates, which are two D_S states, two D_T states, and four quadruplet states For simplicity, we show only the spin states with (1,2) charge configuration in Table 1[34–36], where the spin state in the first (second) bracket indicates the single- (two-) electron spin state in the left (right) QD.

Rate equation

Nuclear spin polarization and the diffusion process were phenomenologically modeled using a rate equation:

$$\frac{dB_{nuc}}{dt} = -B_{nuc}/\tau_N + b_0 P_{flip}/T_{rep}, \quad (1)$$

where τ_N is the nuclear spin diffusion time, b_0 is the Overhauser field change per electron spin-flip, P_{flip} is the nuclear spin flop probability obtained from the Landau–Zener transition probability P_{LZ} and the false initialization probability (see Supplementary Note 5), and T_{rep} is the pulse repetition period. Using Eq. (1), we simulated the polarization-probe sequence shown in Fig. 3 with the experimental parameters including the time required for the amplitude sweep in the leakage probe step.

Data availability

The data that support the findings of this study are available from the corresponding author upon request.

References

1. Chekhovich, E. A. et al. Nuclear spin effects in semiconductor quantum dots. *Nat. Mater.* **12**, 494–504 (2013).
2. Nichol, J. M. et al. Quenching of dynamic nuclear polarization by spin–orbit coupling in GaAs quantum dots. *Nat. Commun.* **6**, 7682 (2015).
3. Petta, J. R. et al. Coherent manipulation of coupled electron spins in semiconductor quantum dots. *Science* **309**, 2180–2184 (2005).
4. Johnson, A. C. et al. Triplet–singlet spin relaxation via nuclei in a double quantum dot. *Nature* **435**, 925–928 (2005).
5. Tartakovskii, A. I. et al. Nuclear spin switch in semiconductor quantum dots. *Phys. Rev. Lett.* **98**, 026806 (2007).
6. Ardenkjær-Larsen, J. H. et al. Increase in signal-to-noise ratio of > 10,000 times in liquid-state NMR. *Proc. Natl Acad. Sci.* **100**, 10158–10163 (2003).
7. Simmons, S. et al. Entanglement in a solid-state spin ensemble. *Nature* **470**, 69–72 (2011).
8. Petta, J. R. et al. Dynamic nuclear polarization with single electron spins. *Phys. Rev. Lett.* **100**, 067601 (2008).
9. Reilly, D. J. et al. Suppressing spin qubit dephasing by nuclear state preparation. *Science* **321**, 817–821 (2008).
10. Bluhm, H., Foletti, S., Mahalu, D., Umansky, V. & Yacoby, A. Enhancing the coherence of a spin qubit by operating it as a feedback loop that controls its nuclear spin bath. *Phys. Rev. Lett.* **105**, 216803 (2010).
11. Foletti, S., Bluhm, H., Mahalu, D., Umansky, V. & Yacoby, A. Universal quantum control of two-electron spin quantum bits using dynamic nuclear polarization. *Nat. Phys.* **5**, 903–908 (2009).
12. Shulman, M. D. et al. Suppressing qubit dephasing using real-time Hamiltonian estimation. *Nat. Commun.* **5**, 5156 (2014).
13. Baugh, J., Kitamura, Y., Ono, K. & Tarucha, S. Large nuclear overhauser fields detected in vertically coupled double quantum dots. *Phys. Rev. Lett.* **99**, 096804 (2007).
14. Ono, K. & Tarucha, S. Nuclear-spin-induced oscillatory current in spin-blockaded quantum dots. *Phys. Rev. Lett.* **92**, 256803 (2004).
15. Nichol, J. M. et al. High-fidelity entangling gate for double-quantum-dot spin qubits. *npj Quantum Inf.* **3**, 3 (2017).
16. Fogarty, M. A. et al. Integrated silicon qubit platform with single-spin addressability, exchange control and single-shot singlet-triplet readout. *Nat. Commun.* **9**, 4370 (2018).
17. Martins, F. et al. Negative spin exchange in a multielectron quantum dot. *Phys. Rev. Lett.* **119**, 227701 (2017).
18. Pioro-Ladrière, M. et al. Electrically driven single-electron spin resonance in a slanting Zeeman field. *Nat. Phys.* **4**, 776–779 (2008).
19. Laird, E. A. et al. Coherent spin manipulation in an exchange-only qubit. *Phys. Rev. B* **82**, 075403 (2010).
20. Hanson, R., Kouwenhoven, L. P., Petta, J. R., Tarucha, S. & Vandersypen, L. M. K. Spins in few-electron quantum dots. *Rev. Mod. Phys.* **79**, 1217–1265 (2007).
21. Yannouleas, C. & Landman, U. Spontaneous symmetry breaking in single and molecular quantum dots. *Phys. Rev. Lett.* **82**, 5325–5328 (1999).
22. Abadillo-Uriel, J. C., Martinez, B., Filippone, M. & Niquet, Y.-M. Two-body Wigner molecularization in asymmetric quantum dot spin qubits. *Phys. Rev. B* **104**, 195305 (2021).
23. Ercan, H. E., Coppersmith, S. N. & Friesen, M. Strong electron-electron interactions in Si/SiGe quantum dots. *Phys. Rev. B* **104**, 235302 (2021).
24. Shapir, I. et al. Imaging the electronic Wigner crystal in one dimension. *Science* **364**, 870–875 (2019).
25. Yannouleas, C. & Landman, U. Symmetry breaking and quantum correlations in finite systems: studies of quantum dots and ultracold Bose gases and related nuclear and chemical methods. *Rep. Prog. Phys.* **70**, 2067–2148 (2007).
26. Pecker, S. et al. Observation and spectroscopy of a two-electron Wigner molecule in an ultraclean carbon nanotube. *Nat. Phys.* **9**, 576–581 (2013).
27. Jang, W. et al. Single-shot readout of a driven hybrid qubit in a gaas double quantum dot. *Nano Lett.* **21**, 4999–5005 (2021).
28. Yannouleas, C. & Landman, U. Molecular formations and spectra due to electron correlations in three-electron hybrid double-well qubits. *Phys. Rev. B* **105**, 205302 (2022).
29. Corrigan, J. et al. Coherent control and spectroscopy of a semiconductor quantum dot wigner molecule. *Phys. Rev. Lett.* **127**, 127701 (2021).
30. Yannouleas, C. & Landman, U. Wigner molecules and hybrid qubits. *J. Phys.: Condens. Matter* **34**, 21LT01 (2022).
31. Reilly, D. J., Marcus, C. M., Hanson, M. P. & Gossard, A. C. Fast single-charge sensing with a rf quantum point contact. *Appl. Phys. Lett.* **91**, 162101 (2007).
32. Barthel, C. et al. Fast sensing of double-dot charge arrangement and spin state with a radio-frequency sensor quantum dot. *Phys. Rev. B* **81**, 161308 (2010).
33. Noiri, A. et al. Radio-frequency-detected fast charge sensing in undoped silicon quantum dots. *Nano Lett.* **20**, 947–952 (2020).
34. Shi, Z. et al. Fast hybrid silicon double-quantum-dot qubit. *Phys. Rev. Lett.* **108**, 140503 (2012).
35. Chen, B.-B. et al. Spin blockade and coherent dynamics of high-spin states in a three-electron double quantum dot. *Phys. Rev. B* **95**, 035408 (2017).
36. Hung, J.-T., Fei, J., Friesen, M. & Hu, X. Decoherence of an exchange qubit by hyperfine interaction. *Phys. Rev. B* **90**, 045308 (2014).
37. Jang, W. et al. Robust energy-selective tunneling readout of singlet-triplet qubits under large magnetic field gradient. *npj Quantum Inf.* **6**, 64 (2020).
38. Meunier, T. et al. High fidelity measurement of singlet–triplet state in a quantum dot. *Phys. status solidi B* **243**, 3855–3858 (2006).
39. Shi, Z. et al. Fast coherent manipulation of three-electron states in a double quantum dot. *Nat. Commun.* **5**, 3020 (2014).
40. Kim, D. et al. Quantum control and process tomography of a semiconductor quantum dot hybrid qubit. *Nature* **511**, 70–74 (2014).
41. Petersson, K. D., Petta, J. R., Lu, H. & Gossard, A. C. Quantum coherence in a one-electron semiconductor charge qubit. *Phys. Rev. Lett.* **105**, 246804 (2010).
42. Kim, D. et al. High-fidelity resonant gating of a silicon-based quantum dot hybrid qubit. *npj Quantum Inf.* **1**, 15004 (2015).
43. Jirovec, D. et al. A singlet-triplet hole spin qubit in planar Ge. *Nat. Mater.* **20**, 1106–1112 (2021).
44. Malinowski, F. K. et al. Spin of a multielectron quantum dot and its interaction with a neighboring electron. *Phys. Rev. X* **8**, 011045 (2018).
45. Hanson, R. et al. Zeeman energy and spin relaxation in a one-electron quantum dot. *Phys. Rev. Lett.* **91**, 196802 (2003).
46. Koppens, F. H. L. et al. Driven coherent oscillations of a single electron spin in a quantum dot. *Nature* **442**, 766–771 (2006).
47. Reilly, D. J. et al. Exchange control of nuclear spin diffusion in a double quantum dot. *Phys. Rev. Lett.* **104**, 236802 (2010).

48. Petta, J. R., Lu, H. & Gossard, A. C. A coherent beam splitter for electronic spin states. *Science* **327**, 669–672 (2010).
49. Deng, C. & Hu, X. Nuclear spin diffusion in quantum dots: effects of inhomogeneous hyperfine interaction. *Phys. Rev. B* **72**, 165333 (2005).
50. Nakajima, T. et al. Coherence of a driven electron spin qubit actively decoupled from quasistatic noise. *Phys. Rev. X* **10**, 011060 (2020).
51. Kim, J. et al. Approaching ideal visibility in singlet-triplet qubit operations using energy-selective tunneling-based Hamiltonian estimation. *Phys. Rev. Lett.* **129**, 040501 (2022).

Acknowledgements

This work was supported by the National Research Foundation of Korea (NRF) grant funded by the Korean Government (MSIT) (No. 2018R1A2A3075438 (D.K.), No. 2019M3E4A1080144 (W.J., J.K., J.P., M.-K.C., H.J., H.J., D.K.), No. 2019M3E4A1080145 (W.J., J.K., J.P., M.-K.C., H.J., H.J., D.K.), No. 2019R1A5A1027055 (D.K.), SRC Center for Quantum Coherence in Condensed Matter RS-2023-00207732 (D.K.), and No. 2023R1A2C2005809 (D.K.)), Korea Basic Science Institute (National Research Facilities and Equipment Center) grant funded by the Ministry of Education (No. 2021R1A6C101B418 (D.K.)), and Creative-Pioneering Researchers Program through Seoul National University (SNU (D.K.)). Correspondence and requests for materials should be addressed to D.K. (dohunkim@snu.ac.kr).

Author contributions

D.K. and W.J. conceived the project. W.J. performed the measurements and analyzed the data. J.K. and H.Jung fabricated the device. J.P., M.C., H.Jang, and S.S. built the experimental setup and configured the measurement software. G.K. and B.K. provided the numerical simulation of the Wigner molecules. V.U. synthesized and provided the GaAs heterostructure. All the authors contributed to the preparation of the manuscript.

Competing interests

The authors declare no competing interests.

Additional information

Supplementary information The online version contains supplementary material available at https://doi.org/10.1038/s41467-023-38649-5.

Correspondence and requests for materials should be addressed to Dohun Kim.

Peer review information *Nature Communications* thanks the anonymous reviewers for their contribution to the peer review of this work.